Contents lists available at ScienceDirect

International Journal of Non-Linear Mechanics

Continuation analysis of overhung rotor bouncing cycles with smooth and contact nonlinearities

Mehmet Selim Akay *, Alexander D. Shaw, Michael I. Friswell

Department of Aerospace Engineering, Swansea University, Bay Campus, Swansea, UK

ARTICLE INFO

ABSTRACT

Time simulation has been widely used when investigating the nonlinear response of rotating machines, due to its relative simplicity. However, this approach is computationally inefficient due to large transient decay times and the need to repeat the analysis for multiple drive speeds and initial conditions, and is incomplete because of its inability to give information about unstable responses. Alternatively, the numerical continuation method can be used to explore the nonlinear behaviour of such systems in a more systematic and efficient way. In rotating machinery, tighter tolerances are valued for efficiency, making the rotor–stator contact phenomenon a priority for research. Various cases including rigid and very compliant contact stiffness models have been investigated in the literature, in many cases showing responses similar to that of smooth nonlinearities such as cubic stiffness. This knowledge has been used in the present study to transform the bifurcation diagram of a simpler nonlinearity (cubic) to a more complex one (contact represented by bilinear stiffness approximated using a tanh formulation) through a homotopy of the nonlinear restoring forces present in the system definition. A 2-dof overhung rotor with gyroscopic effects is used in the investigation of quasiperiodic bouncing cycles that appear periodic in the rotating frame. This work not only provides more insight into the behaviour of nonlinear rotor–stator contact responses, but also demonstrates the numerical continuation method as a potential tool to explore the nonlinear rotating system's response in a more structured manner.

1. Introduction

Nonlinear systems exhibit bifurcations in their response patterns depending on the changes in the parameter space. The rub-impact phenomenon in rotordynamics has similarities to an impact oscillator yet with more complexity arising from the gyroscopic effects and the interaction of different FW and BW modes. The phenomenon has been studied in the fields of turbomachinery, drilling equipment [1], and turbomachinery. Understanding the sustained intermittent rotor-to-stator contact response in rotating machinery is important as it might be dangerous in operating conditions [2]. With the ever-stricter efficiency goals on turbine engines [3], the amplitude of the lateral oscillation has to be confined more effectively. This compels engineers to design tighter clearances for the retainer rings, which in turn increases the possibility of a rotor–stator rub failure. Among the earliest studies where the rub-impact phenomenon in rotating machinery was reported, Johnson [4] reported that for the same rotor speed, various responses could be achievable. Ehrich and O'Connor [5] noted the "hula hoop" motion of the rotor–stator couple. Black [6] used a polar receptance law with dry friction.

The steady state responses of a rotor interacting with the stator can be full annular rubs [7–10]. The responses can also be intermittent contact oscillations that are periodic in stationary frame or in rotating frame, synchronous or sub-synchronous in frequency content. Quasiperiodicity and even chaos are observed, as well as these other types of responses in theoretical studies [11–14] and also in experimental studies [15–19].

One of the features of the contact phenomenon that greatly affects the response is the ratio of the stator stiffness to the rotor linear stiffness. A wide range of stator stiffness levels compared to the rotor's stiffness has been investigated. For example, Shaw et al. [14] investigated soft and rigid stators where the stator stiffness values of 0.1 MN/m and 10 MN/m were used to give stiffness ratios of 1.25 and 125, respectively, for an 80 cm long, 2 cm diameter overhung rotor. Zilli et al. [20] used 1.32 for the stiffness ratio, while Karpenko et al. [21] chose a value of 30 for the stator stiffness to rotor stiffness ratio. Some authors modelled the contact with an impact law definition [22,23]. The impact model with friction resulted in rotating frame periodic orbits [23]; a similar response was also observed in the case of very soft snubber ring stiffness [15].

The results from a wide range of stiffness ratios suggests that intrinsically smooth nonlinearities could generate similar responses to discontinuous stiffness models of the rotor–stator interaction. With this inspiration, our preceding study [24] investigated the softer extreme

---

* Corresponding author.
E-mail addresses: m.s.akay.856478@swansea.ac.uk (M.S. Akay), a.d.shaw@swansea.ac.uk (A.D. Shaw), m.i.friswell@swansea.ac.uk (M.I. Friswell).

Abbreviations

dof	Degree of freedom
HBM	Harmonic balance method
FW	Forward whirl
BW	Backward whirl
DL	Double loop (3:1 internal resonance response)
SL	Single loop (2:1 internal resonance response)
S	Synchronous response (stationary in rotating frame)
PD	Period doubling bifurcation or branch

of the contact phenomenon by replacing the snubber ring stiffness of a 2-dof overhung rotor with gyroscopic effects (the *Zilli system* [20]) by a comparable cubic stiffness. Similar internal resonance responses in the rotating frame to those of Zilli et al. [20] was observed, though Zilli et al. interpreted the motion using phasor diagrams in the stationary frame. A transient decay study was performed by Zilli et al. [20] where rapid slow-down of the rotor resulted in a quasiperiodic motion with a higher probability. This fact was more visible in the bifurcation diagrams of Akay et al. [24] that were obtained using numerical continuation; more transient energy would make the instantaneous response reach the unstable solutions, which is more likely to push the response to settle onto these asynchronous solutions. Rotating frame Campbell plots [14] were used to predict regions of quasiperiodic responses. The study showed the numerical continuation as a superior tool to brute force time simulations in terms of computational efficiency to obtain bifurcation diagrams of rotor systems. Stepped sine sweep tests were also an improvement in terms of obtaining more of a solution branch continuously.

Previously, the emphasis of the rotating frame perspective was stressed by Cole & Keogh [23]. They studied quasiperiodic responses that looks periodic in the rotating frame, due to rotor–stator contact friction. Shaw et al. [14] defined the internal resonance phenomenon in the rotating frame, and generalised the idea to multi-dof models.

Chipato et al. [12,13] studied frictional and gravitational effects on the Zilli system. They found that gravity affected the response of the system only when the shaft stiffness was small. The same authors recently simulated an MDOF rotor with disk and shaft contact [25]. Asynchronous quasiperiodic responses which are periodic in the rotating frame were observed in the MDOF model. Dry friction effects were more pronounced for softer stators due to increased contact duration compared to stiffer stators. Ref. [26] modelled the contact of a non-ideal drive system with 5 dofs and an overhung disk, i.e. neglecting the axial dof. They successfully designed a pinned inner ring to prevent sustained rubbing in experiments. Other complex models based on the finite element method (FEM) formulation were given by [16] where a full-scale test rig was used to analyse partial seal contact. They detected the contact with acoustic signals and a Wheatstone bridge. In the FE model, beam elements with 5 dofs per node and gyroscopic, shear and rotary effects were used. The model was deemed reliable for analysing real machines if the rub is soft and was able to produce experimental responses. Torkhani et al. studied the free rundown of real-scale test rigs experimentally and numerically with good agreement [27]. They did not report subharmonic responses in the models contrary to some other works, e.g. [18]. Wang et al. investigated sudden unbalance on an overhung rotor in experiments and in FE simulations [28]. Floquet theory was used to interpret contact as a time varying constraint stiffness. The sudden unbalance tests showed that the supercritical speeds are more sensitive to the sudden unbalance in terms of relative effect on the transient amplitude. Gyroscopic effects decreased this effect. Gyroscopic effects also caused the first backward whirl mode to be excited upon the sudden unbalance. More recently, Prabish and Krishna studied the multi-disk rubbing response of a two-spool engine

for the fan blade-off scenario [29]. The FE model was established with Timoshenko beams, which was reduced using component mode synthesis. The observed quasiperiodic motions exhibited frequencies at fractions of rotor speed. The approximate time variational method was employed to obtain the response, which was validated by time simulations.

Despite these complex models, understanding of the complex phenomena resulting from the rotor–stator rub-impact requires simpler models to be investigated in a more closely controlled way. Ishida et al. [17] investigated the response patterns of a 4-dof extended Jeffcott rotor (i.e. non-centred disk position) with clearance on one bearing only. Eccentricity of the bearing assembly was added to represent effects such as mounting errors. Numerical and experimental methods produced results with a close match, although the numerical model introduced a small change to the system. Rich response patterns were observed that included 2:1 internal resonance in the rotating frame, although this was expressed in the stationary frame as a combination resonance expression. The paper explained the *entrainment* phenomenon theoretically using the stability of the periodic motion, which is the inclusion of a subharmonic region inside a broader region of self-excited quasiperiodic motion.

The numerical continuation method [30] has been used extensively in the rotordynamics literature in the last two decades. Sundararajan and Noah [31] used continuation in conjunction with the shooting method. Von Groll and Ewins [32] used HBM with continuation on a rotor coupled to a stator with mass. The HBM method they used included subharmonic components to allow the detection of details of rub-impact motion. Alternating time frequency (ATF) steps were used to tune the amplitudes of the harmonic components because of the discontinuous stiffness nonlinearity. Later, Peletan and colleagues worked on the HBM [33,34], and used a quasiperiodic HBM formulation [35], adapting both periodic HBM and the continuation method to the quasiperiodic formulation. Branch switching from periodic responses were left for future research. Another study where HBM and numerical continuation were used together was conducted by Salles et al. [36] on the reduced FE model of an aero-engine with three shafts and four snubber rings. The numerical continuation method was used to find isolated solutions in the bifurcation diagrams, where the asynchronous response was not analysed. Al-Solihat and Behdinan [37] used HBM and continuation methods for analysing the response from a rotor system that is supported by bearings with cubic stiffness and damping.

Other approaches in the analysis of rotor–stator interaction include the following. Numerical normal forms were used by Shaw et al. [11] on the rotating frame internal resonance response of a Zilli system and on a multi-disk FE rotor model, where the fundamental frequency of harmonic expansion was not required beforehand but calculated in the solution process. Nonlinear normal modes, originally developed by [38], were used to define complex nonlinear modes by Laxalde and Thouverez [39], which were then utilised in the analysis of turbomachinery blades with friction interfaces. The concept was used by Hong et al. [40] on a Jeffcott rotor where the negative modal damping of backward whirl motion was found to cause instability, leading to a backward whip motion. Also, Liu and Hong used the complex nonlinear modes of a compressor–turbine unit to analyse the dry whip motion [41]. The modal assurance criteria was used by [25] to identify the modal content of the nonlinear response of an interacting rotor–stator system, where the modal amplitudes of the FFT of the response were compared to the linear eigenvalue solutions of the same system. Backward whirl modes constituted many of the modal components. Piecewise-smooth dynamics was used by Mora et al. [22] to define contact for a Zilli system where the grazing bifurcations of the rub-impact phenomenon were investigated to analyse the onset of the rub-impact fault. A similar method of piecewise-smooth dynamics was used by [42].

In the wider scope of rotor–stator contact, backup bearing impact for magnetically supported shafts were studied [43,44]. Refs. [45,46]
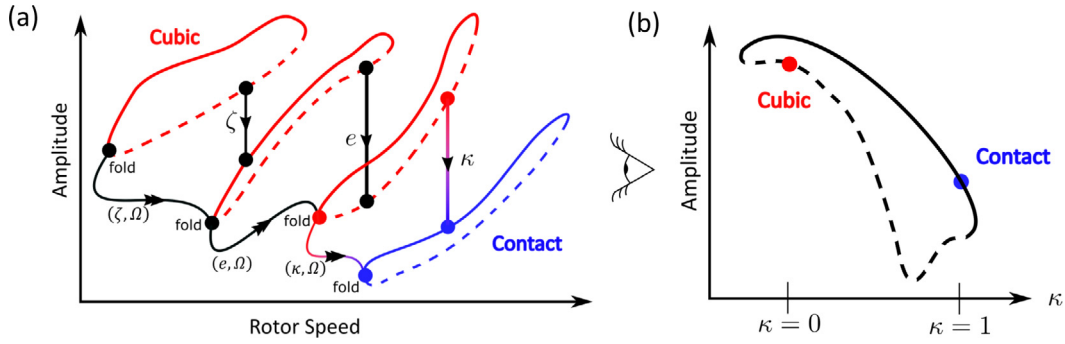
Fig. 1. (a) A representative cubic to contact transition with single parameter method (single arrows, see Fig. 4(a) and (b)) and fold method (double arrows, see Fig. 4(c)). (b) A representative κ homotopy is illustrated in a pair of axes perpendicular to the bifurcation diagram for the single parameter method (see Fig. 4(b)).

investigated grounded nonlinear energy sinks to suppress the motion of a vibrating 4-dof rotor. The nonlinear stiffness used in the study was cubic, but practically obtained using a squirrel cage. Some of the rods constituting the squirrel cage had clearance of varying sizes at one end; as the amplitude of oscillation increased these clearances closed one by one, creating a piecewise-linear stiffness that approximated a cubic stiffness profile. Cubic pedestal stiffness with looseness was studied in an HBM formulation, time integration and experiment by [47], where quasiperiodic motion was seen in addition to subharmonic and multi-period motions. Rotor blades rubbing against the stator were studied by [48] on a disk with wide chord blades, and [49] studied the effect of manoeuvres of a plane on the blade rub phenomenon using a 2-disk aero-engine model, one of which was contacting with the stator.

In the present study of the nonlinear overhung rotor (the Zilli system) shown in Fig. 2, the rotor–stator contact interaction is initially replaced by an isotropic cubic stiffness whose solutions have already been obtained [24]. To explore the characteristics of the system with contact and gain new insights, homotopy continuation (e.g. see [30]) is applied from these cubic stiffness solutions to a hyperbolic tangent function representing a smooth approximation to the discontinuous stiffness as a contact definition. Aside from this nonlinearity homotopy, the continuation method is also applied to investigate different parameter spaces. In the following, Section 2 outlines the theory and the method, with a brief discussion on numerical continuation, and the equations of motion. In Section 3, results are presented with relevant discussion of various cases of damping and unbalance excitations, and the effectiveness of the tanh-contact representation is discussed. In Section 4, conclusions are drawn both on the method and the rub-impact system analysed.

2. Theory and methods

2.1. Numerical continuation

Numerical continuation allows a known solution to be used as the basis to trace a *branch of solutions* or a *solution family*. In the case of *arc-length numerical continuation* [30], which was implemented in the present work, the so-called *folds* or *turning points* (Fig. 1) of a solution can be traced without any numerical issues, regardless of the stability of solution. This contrasts well to a time simulation where an initial condition is simulated in time using e.g., a Runge–Kutta scheme, to converge only onto stable solutions. Furthermore, the numerical checks can spot bifurcations off the main branch, which could more easily be unnoticed in a simulation scheme, unless a computationally expensive basin of attraction study is conducted.

The method states that in the vicinity of a regular point, u_0, satisfying a system of equations of the form $G(u, \lambda) = 0, G : R^n \times R \to R^n$, there is a continuous family of solutions given that $G(u, \lambda)$ is continuously differentiable at this point and the Jacobian $G_u(u_0, \lambda_0)$ is non-singular
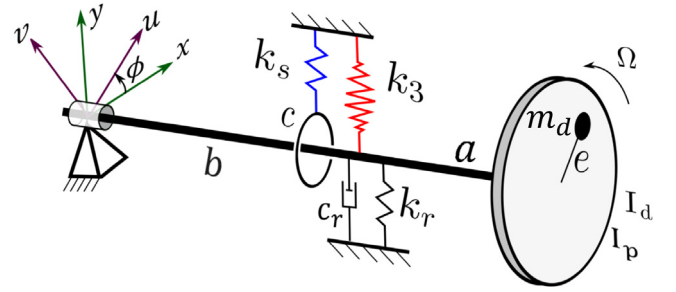

Fig. 2. Schematic drawing of the mechanical system used. In the figure c_r is the damping coefficient, k_r is the linear radial rotor stiffness, k_s is the stator stiffness that engages after a clearance c, k_3 is the cubic stiffness. All stiffness and damping components are **isotropic**. The rotating frame $[u, v]$ has an angle of $\phi = \Omega t$ with the stationary frame $[x, y]$.

(*the Implicit Function Theorem*). Here, λ is the free parameter of the system which is to be changed to investigate the response. Differentiating $G(u, \lambda)$ gives,

$$G_u \frac{du}{d\lambda} + G_\lambda = 0 \quad \to \quad \frac{du}{d\lambda} = -G_u^{-1} G_\lambda \tag{2.1}$$

where G_λ is the derivative of the system with respect to the free parameter, λ. If the Jacobian G_u is singular, i.e. at *fold* points, this equation becomes problematic. However, if λ is appended to the states of the system as a further unknown, $x = (u, \lambda)$, and the parametrisation of the branch uses the arclength of the solution family instead of λ, the folds can be passed. An *arclength* condition expressed as $\dot{x}^T \cdot \dot{x} = \|\dot{x}\|^2 = 1$ is used to augment the system in finite difference form that is multiplied once by the increment of the arclength (the step size), $\Delta s = (s_1 - s_0)$, see Eq. (2.2). This ensures that the extended Jacobian, $G_x = [G_u, G_\lambda]$ is full rank even at folds. Thus,

$$F(x_1, s) = \begin{cases} G(x_1) = 0 \\ (x_1 - x_0)^T \cdot \dot{x}_0 - \Delta s = 0, \quad \|\dot{x}_0\| = 1 \end{cases} \tag{2.2}$$

where the direction vector $\dot{x}_0$ is written with respect to the arclength, s, the sub-scripts *0* and *1* denote the known and the next point to calculate on the solution family, respectively. This next point is initially predicted with a step such as $\left(u_1^{(0)}, \lambda_1^{(0)}\right)^T = (u_0, \lambda_0)^T + (\Delta u_0, \Delta \lambda_0)^T$. A Newton–Raphson correction step, for example, can be implemented on the predicted solution: $F_x\left(x_1^{(v)}\right) \cdot \Delta x_1^{(v)} = -F^{(v)}(x_1)$ with the definition of distance as $\Delta x_1^{(v)} = x_1^{(v+1)} - x_1^{(v)}$ where v designates the vth correction iteration of the next point, x_1. This yields the following Newton–Raphson iteration equation:

$$\begin{bmatrix} G_u(u_1^{(v)}, \lambda_1^{(v)}) & G_\lambda(u_1^{(v)}, \lambda_1^{(v)}) \\ \dot{u}_0^T & \dot{\lambda}_0 \end{bmatrix} \begin{Bmatrix} \Delta u_1^{(v)} \\ \Delta \lambda_1^{(v)} \end{Bmatrix}$$
$$= -\begin{Bmatrix} G(u_1^{(v)}, \lambda_1^{(v)}) \\ \left(u_1^{(v)} - u_0\right) \cdot \dot{u}_0 + \left(\lambda_1^{(v)} - \lambda_0\right) \cdot \dot{\lambda}_0 - \Delta s \end{Bmatrix} \tag{2.3}$$

After the convergence (when the solution is no longer changing with respect to a convergence criteria such as $\frac{\max\left(\Delta u_1^{(\nu)}\right)}{1+\max\left(u_1^{(\nu)}\right)}, \frac{\Delta\lambda_1^{(\nu)}}{1+\lambda_1^{(\nu)}} < \epsilon_u, \epsilon_\lambda$ in AUTO [50]), the next direction vector $\dot{x}_1 = \left(\dot{u}_1, \dot{\lambda}_1\right)$ is determined from the derivation of the system at the new point: $F_x\left(x_1\right) \cdot \dot{x}_1 = \{0,1\}^T$. The new direction vector is normalised to make up the new arclength equation: $\|\dot{x}_1\| = 1$, which is used in the definition of the new system (see Eq. (2.2)) for the calculation of the next point (see Eq. (2.3)).

In the periodic case, u of Eq. (2.3) will be obtained from the discretisation in time of the periodic solution y to the ODE $\dot{y} = T f(y, \lambda)$. There are two additional conditions, namely, periodicity $y(0) = y(1)$ and a phase locking condition such as $P_{phase}(y(0), \lambda) = \dot{y}_k(\tau = 0) = 0$, where k is an arbitrary dimension. Here, T is the true period and the derivatives are with respect to the period-normalised time, τ, defined within $0 < \tau < 1$. Also, for a periodic solution, the period and the free parameter are constant, namely, $\dot{T} = 0$ and $\dot{\lambda} = 0$, respectively. Lastly, adding parametrisation $P_{param}(y(0), \lambda)$ (such as arclength as shown above) and gathering the equations together, one can write,

$$\begin{pmatrix} \dot{y} \\ \dot{T} \\ \dot{\lambda} \end{pmatrix} = \begin{pmatrix} T f(y, \lambda) \\ 0 \\ 0 \end{pmatrix}, \qquad r = \begin{pmatrix} y(0) - y(1) \\ P_{phase}(y(0), \lambda) \\ P_{param}(y(0), \lambda) \end{pmatrix} = 0 \qquad (2.4)$$

The discretisation of this ODE will ultimately result in a system of the form $F = 0$ for which the above discussion of arclength continuation is relevant. The discretisation, as well as the issues of stability and step size, are well discussed in textbooks, such as in [30].

The numerical continuation method was implemented using the open source software AUTO [50], where the stability is calculated based on the work of Fairgrieve and Jepson [51].

2.2. Equations of motion

Eq. (2.6) shows the dimensional nonlinear equations of motion of the 2-dof overhung rotor with a massless shaft in the rotating coordinate frame (Fig. 2). The reason why the rotating frame was selected is that the investigated bouncing solutions are quasiperiodic in the stationary frame, yet periodic in the rotating frame [14].

$$\frac{I_d^o}{a^2}\ddot{V} + \left(-\omega J \frac{I_p - 2I_d^o}{a^2} + c_r\left(\frac{b}{a}\right)^2 1\right)\dot{V}$$
$$+ \left(\omega^2 \frac{I_p - I_d^o}{a^2} 1 + k_r\left(\frac{b}{a}\right)^2 1 + c_r\left(\frac{b}{a}\right)^2 \omega J\right)V + b_{nl} = m_d e\omega^2 \begin{Bmatrix} 1 \\ 0 \end{Bmatrix}$$

$$b_{nl} = (1 - \kappa)b_{cubic} + \kappa b_{snub}$$

$$b_{cubic} = k_3\left(\frac{b}{a}\right)^4 r_c^2 V,$$

$$b_{snub} = \frac{1}{2}\left(\tanh\left(K\left(\frac{r_c b}{a} - c\right)\frac{1}{c}\right) + 1\right)k_s\left(\frac{b}{a}\right)^2\left(1 - \frac{1}{r_c}\frac{ca}{b}\right)V$$

$$(2.5)$$

where

- I_p is the polar moment of inertia of the rotor,
- $I_d^o = I_d + m_d a^2$ is the diametral moment of inertia with respect to the centre of the frame of reference,
- b is the position of all stiffness and damping elements on the rotor (Fig. 2), a is the overhung distance,
- $V = \{u, v\}^T$ is the vector of positions in the rotating frame,
- $r_c = V^T \cdot V$ is the amplitude of the position of the centre of the disk,
- K is the tanh function steepness,
- ω is the rotor speed,
- b_{nl} is the weighted sum of the nonlinear restoring forces from snubber ring stiffness and the cubic stiffness elements.

Table 1
The reference values of the constants that appear in Eq. (2.6) unless otherwise indicated.

Damping ratio	$\zeta = 0.01$
Nondimensional polar moment of inertia	$J_p = 0.143$
Nondimensional disk mass	$m = 0.9$
Nondimensional distance of the eccentric centre of mass	$\varepsilon = 0.353$
Cubic stiffness measure	$\gamma = 0.25$
Stiffness ratio	$\beta = 10$
Tanh-steepness parameter	$K = 150$
Nonlinearity weight	$\kappa = 0$

If Eq. (2.5) is multiplied by $\frac{1}{k_r}\frac{a}{bc}$, the following nondimensional equations of motion can be obtained, which was derived in more detail by [24],

$$U'' + \left(-\Omega J\left(J_p - 2\right) + 2\zeta 1\right)U' + \left(\Omega^2\left(J_p - 1\right)1 + 1 + 2\zeta\Omega J\right)U + f_{nl}$$
$$= m\varepsilon\Omega^2\begin{Bmatrix} 1 \\ 0 \end{Bmatrix}$$

$$f_{nl} = (1 - \kappa)f_{cubic} + \kappa f_{snub}$$

$$f_{cubic} = \gamma r^2 U, \qquad f_{snub} = 0.5\left(\tanh\left(K\left(r - 1\right)\right) + 1\right)\beta\left(1 - 1/r\right)U$$

$$(2.6)$$

The following identities appear in Eqs. (2.5) and (2.6),

$$J = \begin{bmatrix} 0 & -1 \\ 1 & 0 \end{bmatrix}, \quad 1 = \begin{bmatrix} 1 & 0 \\ 0 & 1 \end{bmatrix},$$

$$\gamma = \frac{k_3}{k_r}c^2, \quad \beta = \frac{k_s}{k_r}, \quad \zeta = \frac{c_r b^2}{2I_d^o\omega_n}, \quad m = \frac{m_d a^2}{I_d^o},$$

$$(\cdot)' = \frac{(\cdot)}{\omega_n}, \quad \Omega = \frac{\omega}{\omega_n}, \quad \omega_n^2 = \frac{k_r b^2}{I_d^o}, \quad \bar{c} = \frac{ca}{b}, \quad J_p = \frac{I_p}{I_d^o}$$

$$(2.7)$$

$$U = V\frac{1}{c}, \quad r = \frac{r_c}{c}, \quad \varepsilon = \frac{e}{c}$$

where

- U is the nondimensional position vector in the rotating frame,
- Ω is the nondimensional rotor speed,
- ζ is the damping ratio,
- J_p is the nondimensional polar moment of inertia,
- m is the nondimensional disk mass,
- ε is the nondimensional distance of the eccentric centre of mass,
- $\beta = k_s/k_r$ is the nondimensional measure of snubber-ring stiffness,
- $\gamma = b^2 k_3/k_r$ is the nondimensional measure of cubic stiffness,
- r is the nondimensional vibration amplitude in the rotating frame, $r^2 = U^T \cdot U$.

The definition of the restoring force as a weighted sum of the two nonlinearities allows one to incorporate a new parameter, κ, ranging from 0 to 1 Eq. (2.6). Table 1 gives the constants used to obtain the results in the next section.

2.2.1. Contact definition

The numerical continuation method assumes smoothness of the solutions with respect to the free parameters (see Section 2.1). Therefore, instead of the Heaviside step function, a tanh function was employed, which does not require a correction step (see e.g. [32]). The accuracy of this function is determined by the tanh-steepness parameter, K.

In the definition of the tanh-contact formulation, care must be taken to ensure accuracy and efficiency at the contact amplitude, where a fictitious negative restoring force is generated, see Fig. 3(b). For the same ratio between the (β, K) pair (e.g. (5,50) and (10,100) pairs), the fictitious force amplitude is the same, but the width of the affected zone is different. Also, observing the red lines' cascade, one can see that for a given β, the increase of K decreases the amplitude and the affected zone width (see Fig. 3) together. This artificial effect of the sigmoid function
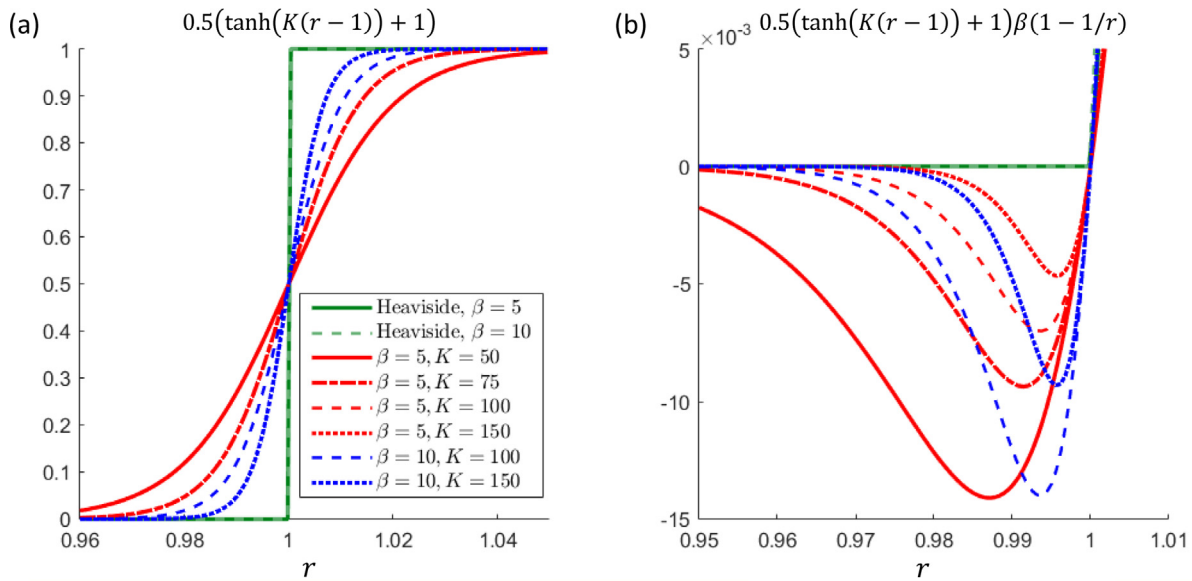
Fig. 3. (a) Hyperbolic tangent function for various β and K value pairs. This paper used $\beta = 10, K = 150$. (b) The returning force at the contact amplitude generated by the tanh-contact definition. The legend applies to both figures. (For interpretation of the references to colour in this figure legend, the reader is referred to the web version of this article.)
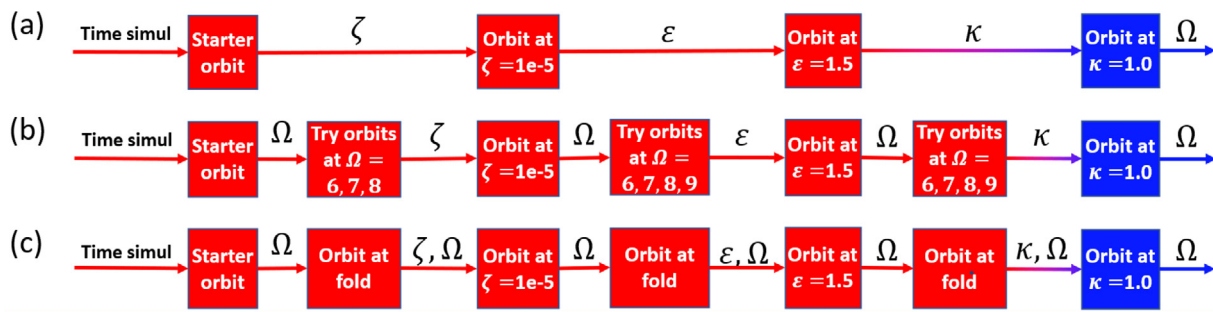

Fig. 4. The flow of runs. (a) A direct and unlikely single parameter flow. (b) Single parameter flow with added Ω runs for more flexibility on the parameter space. (c) Fold-continuation flow. The arrows show the continuation runs and obtained solution families, and the homotopy process in the case of κ. The red and blue boxes show the sampled orbits of cubic and contact cases, respectively. The continuation of ζ and ε are optional in the exploration of the new nonlinearity for the system. (For interpretation of the references to colour in this figure legend, the reader is referred to the web version of this article.)

was more pronounced than tanh for the same values of β and K, which is not presented here. Therefore, the tanh function was adopted in the present study.

The chosen value of K was determined by comparing the bifurcation diagrams from the tanh-contact model to that from a Heaviside-contact model (Fig. 3) using the *ode45* function of MATLAB (RK4(5) scheme of Dormand and Prince [52]). This resulted in the selection of $K = 150$ for $\beta = 10$ (see Fig. 3).

2.3. Homotopy from smooth to contact nonlinearity

The parameter κ is used to switch the system response from cubic nonlinearity ($\kappa = 0$) to the contact nonlinearity ($\kappa = 1$), as shown in Fig. 1. As a first approach, a homotopy process can be applied on a starter orbit generated using the cubic nonlinearity, to change it to the response of a system with contact nonlinearity, while optionally adding other parameter changes as shown in Fig. 4(a). This might result in a failure if a different state of the parameter space is needed for κ to reach 1. For example, for the given values of ζ, ε and Ω, a κ homotopy might reach a value of $\kappa = 0.8$, make a fold, and then decrease the values of κ. Thus, as in Fig. 4(b), additional continuation in Ω may be necessary.

To avoid this trial and error approach, Fig. 4(c) shows that a more direct alternative is to trace the fold point of the cubic nonlinearity (if

a fold point is present in the interested range) via a fold-continuation in two free parameters. In the runs, the most intuitive parameter is the rotor speed, and the main investigation concerns the bifurcation diagrams with respect to the rotor speed. Therefore, this additional parameter was selected as Ω for both optional parameter change runs and for homotopy of the nonlinearity. The approaches in Fig. 4(b) and Fig. 4(c) were applied successfully, despite the greater difficulty in the numerical convergence of the fold-continuation method (Fig. 4(c)) in the low ζ cases. When the damping approaches zero, the periodic solutions' isolation is not guaranteed, hence the tangent vector struggles to resolve. In order to help the convergence, the minimum arclength step size was decreased from 0.05 to 0.0001, the number of Newton-Chord iterations was increased from 5 (default) to 7, out of which the Newton iterations were increased from 3 (default) to 5. Also, the relative convergence criterion was relaxed from 10^{-6} to $3 \cdot 10^{-6}$ for both the continuation parameters and the solution components, i.e., the states $\{U, \dot{U}\}^T$ of Eq. (2.6).

3. Results and discussion

Fig. 5 shows the investigated 3:1 and 2:1 internal resonance responses in the rotating frame. These responses were named double loop
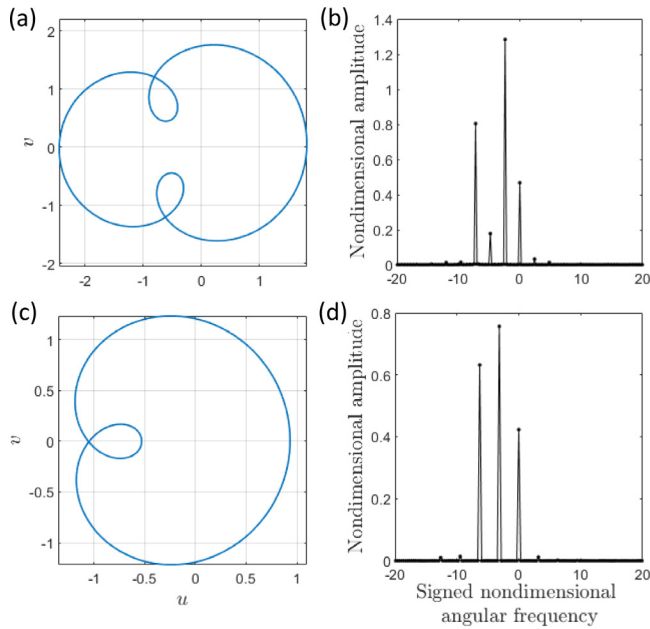
Fig. 5. At a nondimensional rotor speed of $\Omega = 5.0$; (a) a sample 3:1 (DL) internal resonance response in the rotating frame from tanh-contact, and (b) its signed frequency content, (c) a sample 2:1 (SL) internal resonance response in the rotating frame, and (d) its signed frequency content. Negative frequencies indicate a backward whirl in the present frame of reference, which is rotating with Ω. The DC components result from the unbalance excitation that is a constant force in this rotating frame.
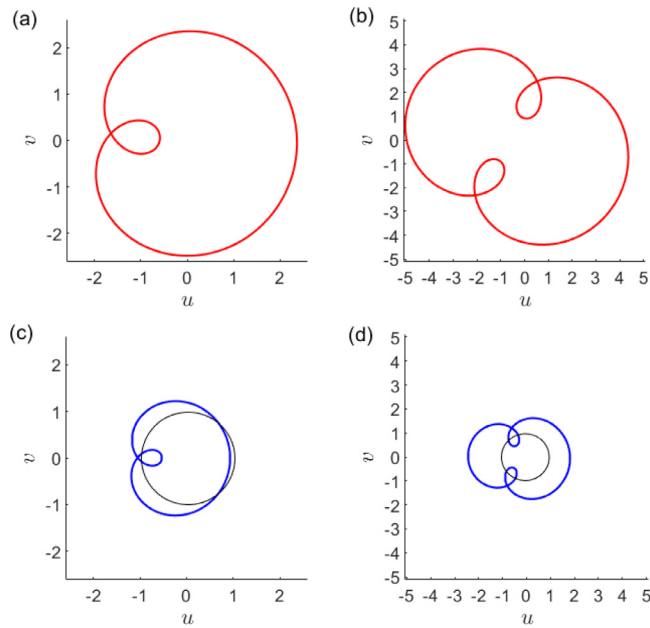
Fig. 6. Orbits at $\Omega = 5.0$ corresponding to responses of cubic (a) SL and (b) DL, tanh-contact (c)SL and (d) DL responses. Black circles in (c) and (d) show the contact level for the tanh-contact system (see Eq. (2.6)). Other parameters are default according to Table 1.

(DL) and single loop (SL), respectively, due to their appearance. The frequency content of the SL and DL responses are shown in Fig. 5(d) and (b), respectively, which were calculated from the complex signed frequency content, $\boldsymbol{U}_\omega$, obtained from the DFT as,

$$\boldsymbol{U}_\omega(k) = \frac{1}{N}\boldsymbol{U}^*(t) \cdot \mathrm{e}^{-j2\pi f_k t}, \quad \boldsymbol{U}^*(t) = \{1, -j\} \cdot \boldsymbol{U}(t),$$

$$f_k = \left(-\left(\frac{N}{2}+1\right)+k\right)\frac{f_s}{N}, \quad k = 1, 2, \ldots, N, \tag{3.1}$$

N is the data length and is even.

where t is the vector of N time points of an orbit's trajectory data and f_s is the sampling rate. The shape of the complex transform, $\{1, -j\}$, is selected so that a forward whirl motion is associated with a positive whirl frequency, ω, using $Re\left(\left\{\begin{array}{c}1\\-j\end{array}\right\}e^{+j\omega t}\right)$, given the Fourier transform convention with a negative sign in the exponential ($\mathrm{e}^{-j2\pi f_k t}$). Here, the $\boldsymbol{U}(t)$ matrix stores in its columns the nondimensional positions in the rotating frame at different times, and the rows are the corresponding time series to each nondimensional position; $\boldsymbol{U}^*(t)$ is a vector of the time series of the complex nondimensional position in the rotating frame — note the number of dof is two for the system investigated. The nondimensional frequency amplitudes in Fig. 5(b) and (d) are the magnitude of the vector $\boldsymbol{U}_\omega$. The DC components here indicates the response due to the unbalance forcing, which is a constant force in rotating frame. Converged internal resonance responses of SL and DL in the rotating frame from the cubic stiffness formulation were used to start the continuation process. This corresponds to the first arrow and the first box in Fig. 4. An orbit on this branch was used to start the continuation of the homotopy parameter, κ, switching to the contact definition, without optional parameter changes of ζ and ε (Fig. 4(b)).

Similarity of the responses from the cubic formulation and the contact formulation could be observed in Fig. 6. The orientations of the loop of these orbits are different in the two systems, which might be linked to the delayed engagement of the tanh-contact nonlinearity above the amplitude level of the clearance compared to the cubic case where the nonlinearity is active at all amplitude levels. Apart from this, the orbits do not show qualitative difference.

The analysis here corresponds to the values given in Table 1, which were chosen by [24] to constitute a model that is comparable to that of [20].

The results for the cubic case are shown in Fig. 7(a). For all the plots including those in Fig. 7, continuous and dashed lines show stable and unstable response branches, respectively. The first thing to notice is the difference of the stiffening response between the two nonlinearities. All branches of the cubic nonlinearity bifurcation diagram (Fig. 7(a)) settle onto a constant inclination as the amplitude of oscillation increases because the nonlinear force increases with the amplitude of oscillation. Therefore, the stiffening effect is present at all amplitude levels in the cubic nonlinearity. All branches of the tanh-contact nonlinearity have a strong stiffening effect in the lower amplitude oscillations with contact just above the amplitude level of 1, even manifested on the synchronous (S) branch with a pronounced kink. However, the relative effect of the nonlinearity decreases as the severity of contact increases. This difference can be attributed to the fact that the cubic nonlinearity is present at each amplitude level, whereas the tanh-contact nonlinearity is linear below contact and converges towards linear behaviour at high amplitudes since the effect of the stiffness change becomes less significant. Note that in Fig. 7 (as well as in Fig. 10 and Fig. 12) the S and SL branches do not close within the shown range of rotor speed and amplitude. It should be noted that the out of balance force rises with the square of the drive speed, and it is thought that therefore these solution branches are unbounded. For the system in Eq. (2.6) this has been validated up to $\Omega = 100$ with parameter values in Table 1.

As shown in Fig. 8, the lowest amplitude level for the cubic SL branch is below the contact level; after the nonlinearity switch, the lowest point moves upward above the contact level, because below the contact amplitude, there is no nonlinearity to produce these internal resonance responses.

In the contact bifurcation diagram (Fig. 7(b)), the low amplitude periodic response is mostly unstable. However, a small region between the nondimensional rotor speeds of 4.4 – 4.8 exists, where the unstable periodic orbits of SL might push the transitional response to the DL stable periodic orbits.

In Fig. 7, period doubling bifurcations can be seen on the tanh-contact model, towards the lower amplitudes, which are zoomed in Fig. 9(a). Fig. 9(b) shows the SL period doubling region, where secondary period doubling bifurcation is visible. These period doubling
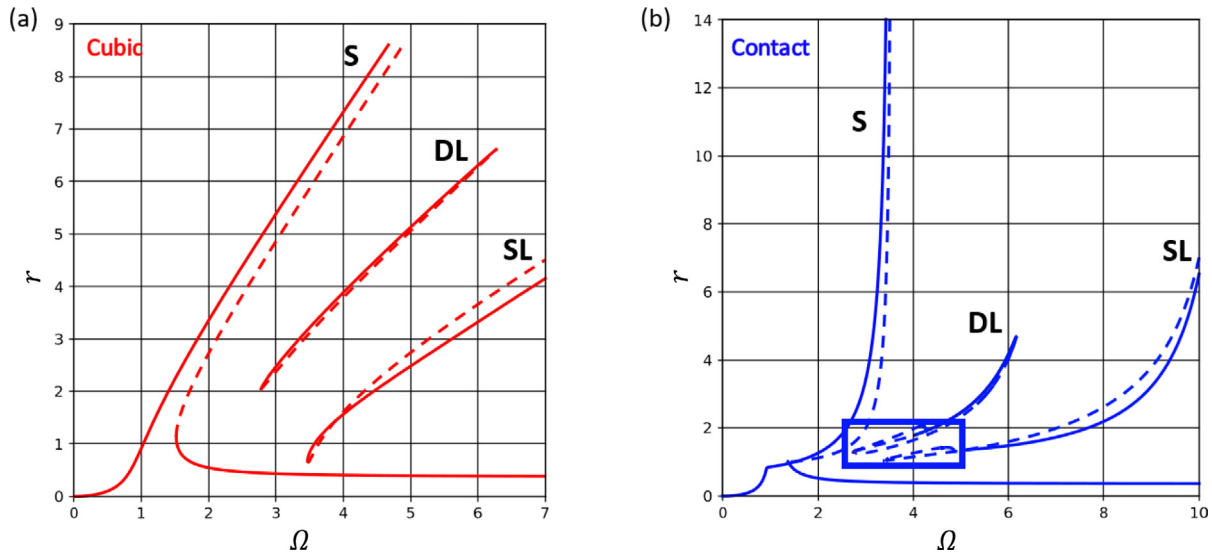
Fig. 7. The transform of the bifurcation diagram in (a) the cubic nonlinearity (red) to that of (b) the contact nonlinearity (blue). The zoomed view of the blue rectangular zone is shown in Fig. 9(a). (For interpretation of the references to colour in this figure legend, the reader is referred to the web version of this article.)
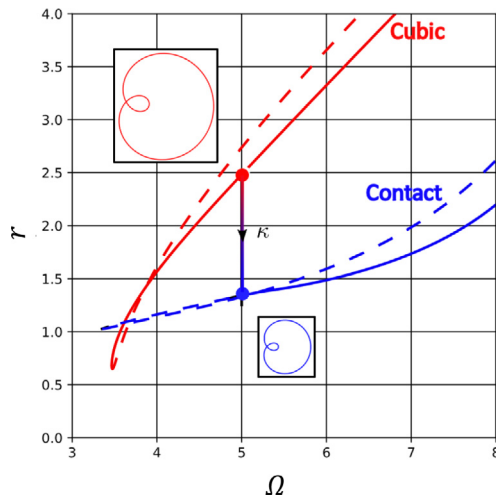

Fig. 8. Closer view of the homotopy of SL periodic solutions. Small orbits are from Fig. 6.

responses are only stable at a very narrow rotor speed band; therefore, it might be unlikely to obtain these solutions in a real-world scenario. Nevertheless, in the brute force time simulation period doubling bifurcations were captured, as shown in Fig. 9(c). Note that, in the time simulations only the stable solutions are converged and the diagram is not as smooth as that obtained from the numerical continuation process (Fig. 9(b)), because some of the responses are converged onto DL or S branches, breaking the PD-branches' integrity. One can mitigate the problem when sweeping in terms of Ω in time simulations by using the end datum of a trajectory as the initial condition for the next Ω, which is shown on the DL PD solutions in Fig. 9(d). More discussion on the comparison of time simulation and numerical continuation can be found in recent work [24]. Lastly, the PD cascade could indicate a chaotic behaviour despite the fact this was not experienced in the time simulations [53].

3.1. The case of low damping

To further explore the behaviour of the new nonlinearity, the original system parameters can be altered before the homotopy of the

nonlinearity. One can investigate the response of the system under a different damping case, which can instantaneously change [54]. In Fig. 10, a damping ratio of $\zeta = 1e-5$ was used to investigate the low damping systems of both nonlinearities comparatively. In addition to the phenomena observed in Fig. 7, the zoom view at the lower amplitude ends of the DL and SL branches in Fig. 11 show that low damping ensures that periodic solutions can be achieved at lower amplitudes levels, closing the gap between the synchronous and asynchronous solutions. This would allow smaller perturbations of the synchronous solution to end up on the periodic solution branches for both nonlinearities more easily. However, since the contact nonlinearity is absent below the contact level, the closing of this gap is confined to right above the contact level, thereby requiring more disturbance of the synchronous solutions to settle onto periodic solutions.

3.2. The case of low damping and high unbalance

The unbalance excitation was increased by setting the eccentricity value greater than the contact clearance, $\varepsilon = 1.5$, while the damping of the systems was retained at $\zeta = 1e-5$. Compared to Figs. 10 and 11, in Fig. 12 the bifurcation diagram of the cubic nonlinearity looks qualitatively identical to the previous case (Fig. 11) except that the amplitudes of oscillation are increased and the internal resonance is moved towards higher frequencies. However, the bifurcation diagram for the contact model shows a closer resemblance to the cubic case, this time. As can be seen in Fig. 12(b), the closing of the contact synchronous and asynchronous solutions is clearly visible. As seen in the cubic nonlinearity, the higher unbalance pushed the region of internal resonance to higher frequencies. However, since the nonlinearity decreases with amplitude in the tanh-contact nonlinearity, the periodic solution families straighten. This phenomenon twisted the DL branch (Fig. 13) so much that a new stable zone formed below the main stable zone. This indicates that the same solution family can generate different amplitude solutions of the same nature within the investigated rotor speed region, breaking an intuition of having the stable solutions of the same solution family located adjacent, for example, in a stepped sine test.

3.3. Tanh-contact

The selection of the steepness, K, of the hyperbolic tangent function was found to be important to avoid contamination of the bifurcation diagram with non-realistic effects. As pointed out in Section 2.2, the
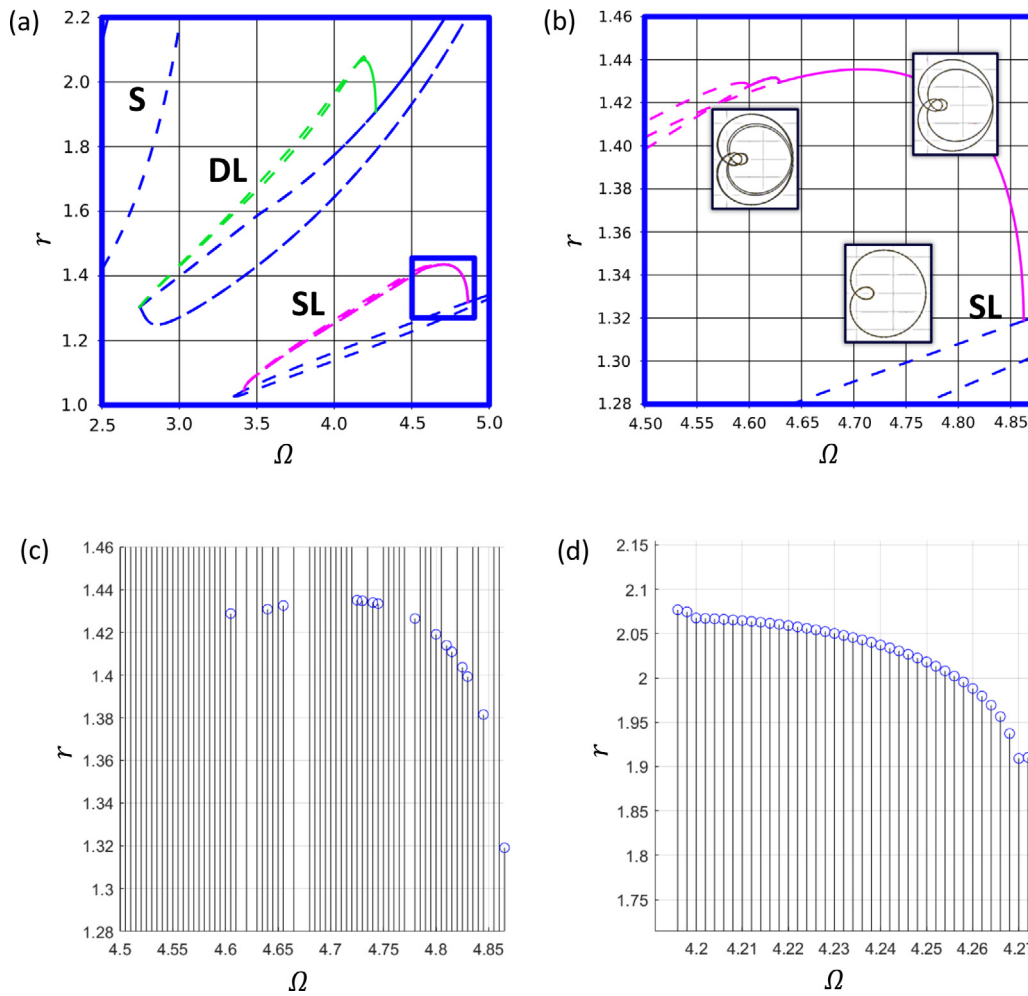
Fig. 9. Period doubling (PD) bifurcation diagrams of tanh-contact model. (a) Zoom view at the blue rectangle in Fig. 7(b) and (b) at the blue rectangle inside (a). (c) Time simulation results of SL solutions. (d) Stepped sine sweep results of DL solutions.
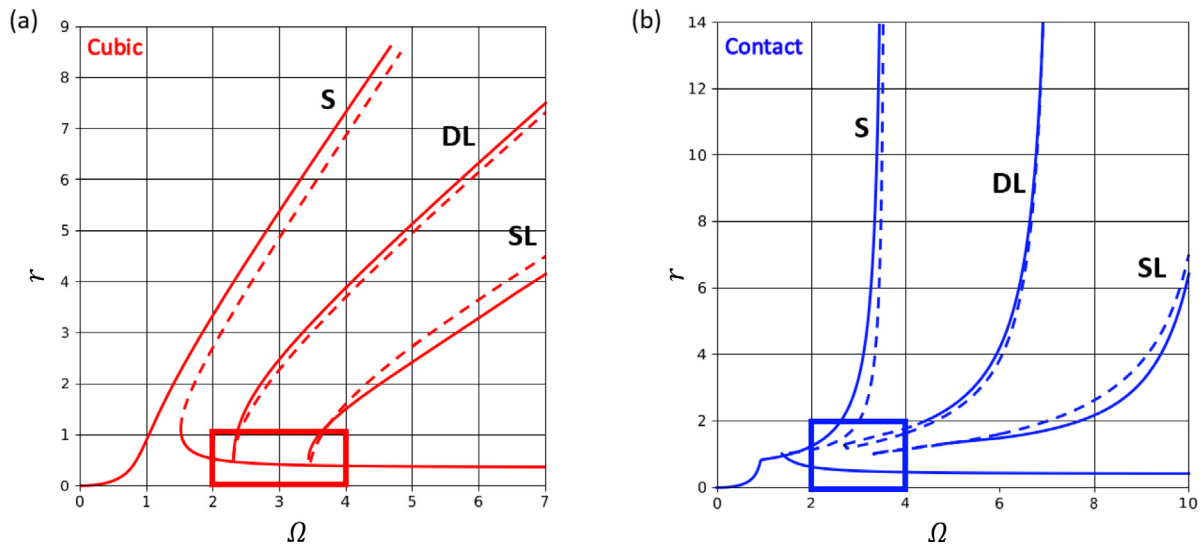

Fig. 10. Bifurcation diagrams that correspond to a very low damping ratio value ($\zeta = 1e - 5$) of (a) the cubic and (b) contact nonlinearities. The zoomed views of the red and blue rectangles in (a) and (b) are shown in Fig. 11(a) and (b), respectively. (For interpretation of the references to colour in this figure legend, the reader is referred to the web version of this article.)

value of K was determined so that the bifurcation diagrams of the time simulations of the tanh-contact model overlapped with that of the Heaviside step functions. This indeed eliminated most of the fictitious response. However, for certain values of the parameters and a value of tanh-steepness smaller than the validated value, the effect of the tanh-contact being a smooth approximation of the contact was visible.
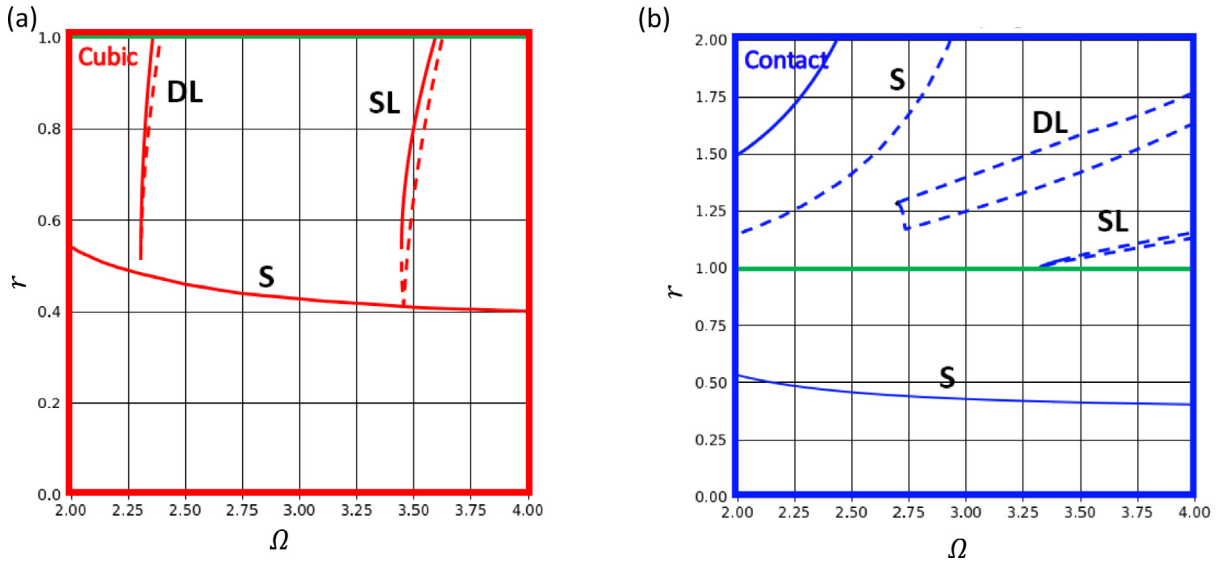
Fig. 11. Low damping case. Zoom view of Fig. 10 at the red and blue windows therein. (For interpretation of the references to colour in this figure legend, the reader is referred to the web version of this article.)
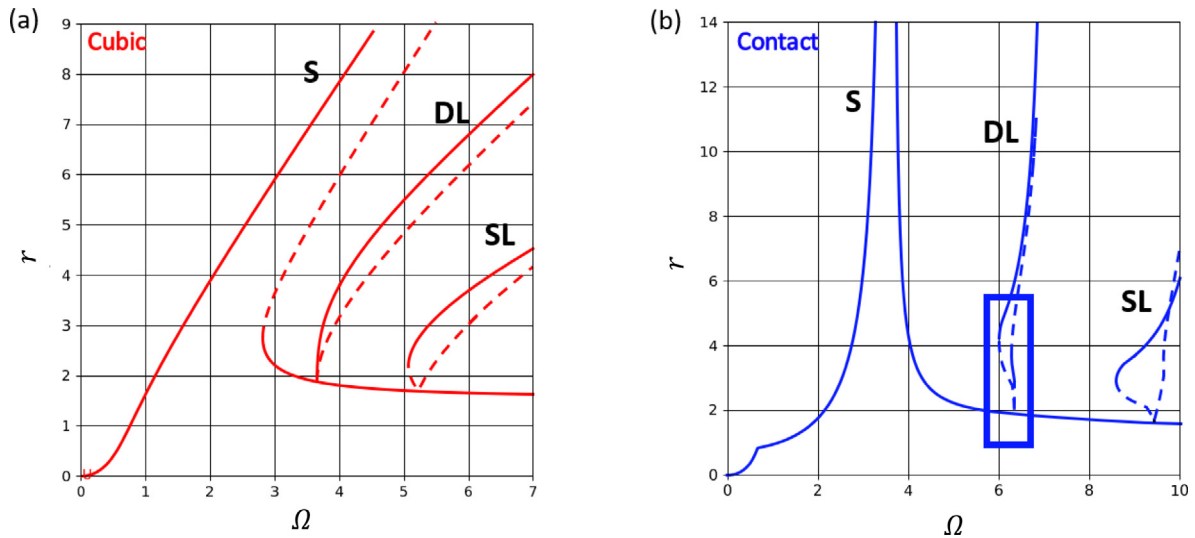

Fig. 12. Bifurcation diagrams that correspond to low damping, high forcing case for (a) the cubic, and (b) the contact nonlinearities.
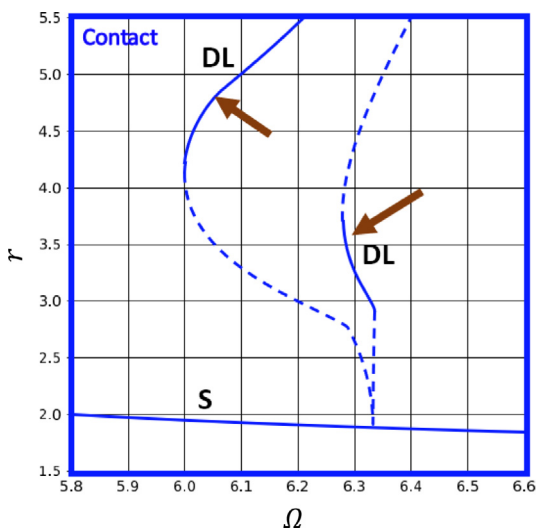

Fig. 13. Low damping, high forcing case. Zoom view at the blue window in Fig. 12. (For interpretation of the references to colour in this figure legend, the reader is referred to the web version of this article.)

Fig. 14 shows two such cases. In Fig. 14(a) there are soft kinks below the contact amplitude, although these would be located at the contact amplitude if it was a true discontinuous stiffness. Even an unstable region is visible between the fold points on the left-hand branch of S solutions (Fig. 14(a)). In Fig. 14(b), one can see the periodic solution family around and below the amplitude of contact. The numerical continuation continued right onto this new solution family for a certain combination of accuracy constants of the runs. However, the fact that this jump occurred shows that they are related to the actual periodic solutions. Nevertheless, the solution was not reliable for the tanh-steepness values, K less then validated by the comparative brute force simulations.

The reason follows from Fig. 3(b), where the restoring force due to the contact definition is plotted. The tanh-contact restoring force below the point of contact has a false negative value in a small region of oscillation amplitude. This means that the solution is pushed downward (towards a lower amplitude) in this region while no force should have been present from the contact. However, the increase of the tanh-steepness decreases this effect considerably, by decreasing the affected amplitude region (on the x-axis of the plot) and shrinking the fictitious restoring force amplitude (on the y-axis of the plot). For the values of $\beta = 10$ and $K = 150$, no such effects were observed in the practical scale, that is, compared to the step size of Ω in the continuation runs.
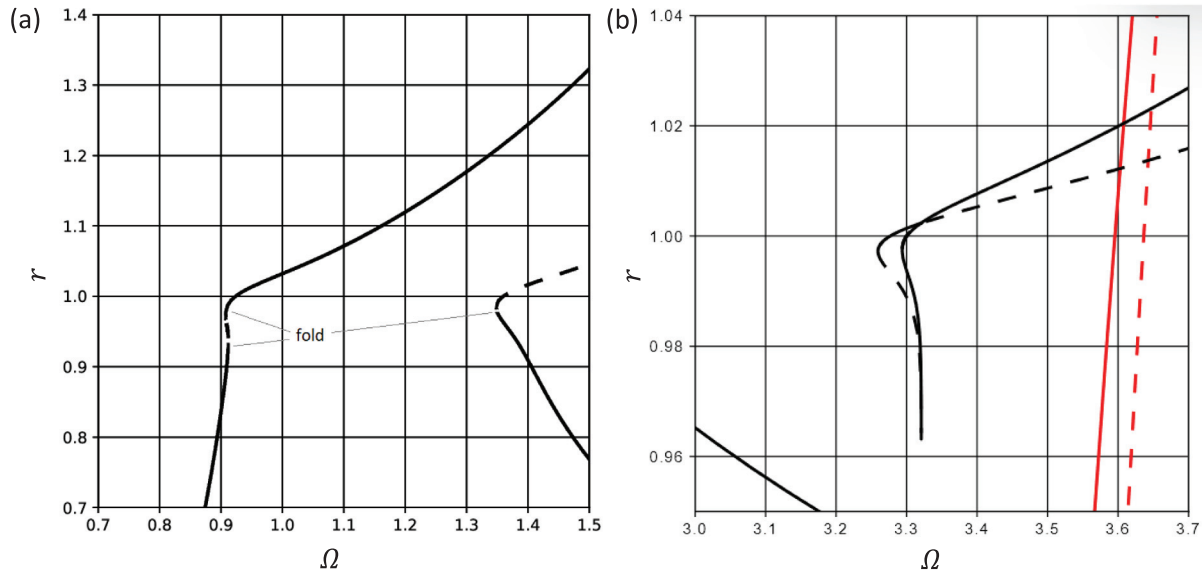
Fig. 14. The fictitious parts of the bifurcation diagram. (a) Smoothing at the kink of the synchronous solution branches for a stiffness ratio of $\beta = 6$ and $K = 30$, a value lower than the validated value of $K = 90$. (b) The fictitious periodic solution family appeared around and below the contact amplitude when $\zeta = 1e-5$ and $\varepsilon = 0.8$. The red solution family shows the cubic case. Other parameters are given in Table 1. (For interpretation of the references to colour in this figure legend, the reader is referred to the web version of this article.)

4. Conclusions

In this paper, a new concept of making the homotopy from one nonlinearity to the other was studied. In the paper, the method was demonstrated on a smooth modification of the *Zilli system* [20] that features a tanh-contact stiffness nonlinearity. The numerical continuation method was employed in the process of changing the parameters of the original cubic-stiffness model, as well as in the homotopy of the nonlinearity weight, κ, that transitions from the cubic to the tanh-contact nonlinearity. The method appears to be a potentially powerful tool for the investigation of more complex nonlinearities starting from a simpler and smoother case. The results were in agreement with the simulations, which were used to validate the contact stiffness. The following conclusions can be drawn:

On the method:

The whole bifurcation diagram can be computed quickly using numerical continuation, including the unstable regions that convey useful information on the response of the system. The user of the method, however, has to note the considerable time needed to setup the correct accuracy constants (in AUTO [50]) adjusting the discretisation and tolerances for computational accuracy and efficiency, such as the maximum and minimum step sizes, the mesh interval count and its adaptation rate, the accepted solution accuracy and so on.

Nonlinear force homotopy made the investigation of the new nonlinearity possible without any prior knowledge on the new system.

The method is useful particularly when the known response belongs to a simple smooth nonlinearity such as a geometrical nonlinearity such as a cubic stiffness instead of a discontinuous stiffness, and shows similar responses to those from the new nonlinearity. The cubic nonlinearity was shown to be such a case in a preceding study [24].

However, more complex nonlinearities can give more complex bifurcation diagrams, that are not easily obtainable from a solution of the simpler system. As such, only the responses that are related in both systems can be analysed in the presented method. For example, a 2:1 internal resonance response in the cubic system cannot result in a branch of 3:2 internal resonance responses in the contact system. However, the responses of the 2:1 (SL) and 3:1 (DL) solutions are quite common in the literature on different systems. If the forcing and damping are zero, the synchronous amplitude goes to zero except that the main backbone is

rooted at the main resonance, and the asynchronous solution branches make up backbone curves. This, in an amplitude-rotor speed bifurcation diagram, would combine the synchronous and asynchronous solutions at the rotating frame Campbell diagram-predicted internal resonance points. However, at the 0-amplitude points where those synchronous and asynchronous solutions meet, the periodicity and morphology of the solutions would be different. This study is left for future research.

Contrary to the approaches in the field of rotordynamics such as those with HBM and shooting method formulations, the direct approach using the system of equations with the tanh-contact definition was straightforward while maintaining a good level of accuracy when compared to the time simulations. The selection of the tanh-contact smooth approximation of the discontinuous stiffness nonlinearity was useful in terms of the ease of setup of the method, not necessitating a correction scheme for the correct calculation of contact forces. Nonetheless, the tanh steepness (accuracy) has to be decided for accuracy around the contact level to avoid prediction of fictitious responses. The solution procedure has the system of equations in first order form, although they need to be discretised to fit into this continuation method. The sophisticated adaptive mesh formulation of AUTO worked well in the non-smooth approximation of the contact discontinuity. In the HBM formulation, one would have the defining factor of the number of equations solved as the harmonics included.

On the dynamics of the system:

Some insight of the dynamics of the system was developed.

The loss of proper damping could make the synchronous unbalance response jump to the periodic (quasiperiodic in the stationary frame) solutions more readily.

The increased unbalance excitation pushed the periodic response higher in amplitude, into the more linear regions of contact nonlinearity. This made the stiffening effect less pronounced in the periodic branches, straightening them in the bifurcation diagrams. As this happened, a new stable solution zone emerged on the DL branch in addition to the regular stable zone. This means that the same pattern of solutions can be observed at different amplitudes.

CRediT authorship contribution statement

Mehmet Selim Akay: Conceptualization, Methodology, Software, Writing – original draft. **Alexander D. Shaw:** Conceptualization, Methodology, Project administration, Software, Supervision, Writing – review

& editing. **Michael I. Friswell:** Conceptualization, Project administration, Supervision, Writing – review & editing.

Declaration of competing interest

The authors declare that they have no known competing financial interests or personal relationships that could have appeared to influence the work reported in this paper.

References

[1] B. Saldivar, I. Boussaada, H. Mounier, S. Mondié, S.I. Niculescu, An overview on the modeling of oilwell drilling vibrations, IFAC Proc. Vol. 47 (3) (2014) 5169–5174, http://dx.doi.org/10.3182/20140824-6-ZA-1003.00478.

[2] G. Jacquet-Richardet others, Rotor to stator contacts in turbomachines, Rev. Appl. Mech. Syst. Signal Process. 40 (2) (2013) 401–420, http://dx.doi.org/10.1016/j.ymssp.2013.05.010.

[3] S. Ahmad, Rotor casing contact phenomenon in rotor dynamics — Literature survey, J. Vib. Control 16 (9) (2010) 1369–1377, http://dx.doi.org/10.1177/1077546309341605.

[4] D.C. Johnson, Synchronous whirl of a vertical shaft having clearance in one bearing, J. Mech. Eng. Sci. 4 (1) (1962) 85–93, http://dx.doi.org/10.1243/jmes_jour_1962_004_012_02.

[5] F.F. Ehrich, J.J. O'Connor, Stator whirl with rotors in bearing clearance, J. Eng. Ind. 89 (3) (1967) 381–389, http://dx.doi.org/10.1115/1.3610057.

[6] H.F. Black, Interaction of a whirling rotor with a vibrating stator across a clearance annulus, J. Mech. Eng. Sci. 10 (1) (1968) 1–12, http://dx.doi.org/10.1243/jmes_jour_1968_010_003_02.

[7] Y.S. Choi, Investigation on the whirling motion of full annular rotor rub, J. Sound Vib. 258 (1) (2002) 191–198, http://dx.doi.org/10.1006/jsvi.5091.

[8] X. Dai, Z. Jin, X. Zhang, Dynamic behavior of the full rotorstop rubbing: Numerical simulation and experimental verification, J. Sound Vib. 251 (5) (2002) 807–822, http://dx.doi.org/10.1006/jsvi.2001.3998.

[9] D.E. Bently, J.J. Yu, P. Goldman, A. Musynska, Full annular rub in mechanical seals, part I: Experimental results, Int. J. Rotat. Mach. 8 (5) (2002) 319–328, http://dx.doi.org/10.1155/S1023621X02000301.

[10] A.R. Bartha, Dry Friction Backward Whirl of Rotors Doctor of Technical Sciences Doctoral Thesis, Swiss Federal Institute of Technology, 2000.

[11] A.D. Shaw, A.R. Champneys, M.I. Friswell, Normal form analysis of bouncing cycles in isotropic rotor stator contact problems, Int. J. Mech. Sci. 155 (2019) 83–97, http://dx.doi.org/10.1016/j.ijmecsci.2019.02.035.

[12] E. Chipato, A.D. Shaw, M.I. Friswell, Frictional effects on the nonlinear dynamics of an overhung rotor, Commun. Nonlinear Sci. Numer. Simul. 78 (2019) http://dx.doi.org/10.1016/j.cnsns.2019.104875.

[13] E. Chipato, A.D. Shaw, M.I. Friswell, Effect of gravity-induced asymmetry on the nonlinear vibration of an overhung rotor, Commun. Nonlinear Sci. Numer. Simul. 62 (2018) 78–89, http://dx.doi.org/10.1016/j.cnsns.2018.02.016.

[14] A.D. Shaw, A.R. Champneys, M.I. Friswell, Asynchronous partial contact motion due to internal resonance in multiple degree-of-freedom rotordynamics, Proc. Math. Phys. Eng. Sci. 472 (2192) (2016) 20160303, http://dx.doi.org/10.1098/rspa.2016.0303.

[15] E.T. Chipato, A.D. Shaw, M.I. Friswell, R. Sánchez Crespo, Experimental study of rotor-stator contact cycles, J. Sound Vib. 502 (2021) http://dx.doi.org/10.1016/j.jsv.2021.116097.

[16] P. Pennacchi, N. Bachschmid, E. Tanzi, Light and short arc rubs in rotating machines: Experimental tests and modelling, Mech. Syst. Signal Process. 23 (7) (2009) 2205–2227, http://dx.doi.org/10.1016/j.ymssp.2009.03.008.

[17] Y. Ishida, M. Inagaki, R. Ejima, A. Hayashi, Nonlinear resonances and self-excited oscillations of a rotor caused by radial clearance and collision, Nonlinear Dynam. 57 (4) (2009) 593–605, http://dx.doi.org/10.1007/s11071-009-9482-3.

[18] F. Chu, W. Lu, Experimental observation of nonlinear vibrations in a rub-impact rotor system, J. Sound Vib. 283 (3-5) (2005) 621–643, http://dx.doi.org/10.1016/j.jsv.2004.05.012.

[19] Y. Ishida, I. Nagasaka, T. Inoue, S. Lee, Forced oscillations of a vertical continuous rotor with geometric nonlinearity, Nonlinear Dynam. 11 (2) (1996) 107–120, http://dx.doi.org/10.1007/BF00044997.

[20] A. Zilli, R.J. Williams, D.J. Ewins, Nonlinear dynamics of a simplified model of an overhung rotor subjected to intermittent annular rubs, J. Eng. Gas Turb. Power 137 (6) (2015) http://dx.doi.org/10.1115/1.4028844.

[21] E.V. Karpenko, M. Wiercigroch, E.E. Pavlovskaia, R.D. Neilson, Experimental verification of Jeffcott rotor model with preloaded snubber ring, J. Sound Vib. 298 (4–5) (2006) 907–917, http://dx.doi.org/10.1016/j.jsv.2006.05.044.

[22] K. Mora, A.R. Champneys, A.D. Shaw, M.I. Friswell, Explanation of the onset of bouncing cycles in isotropic rotor dynamics; A grazing bifurcation analysis, Proc. Math. Phys. Eng. Sci. 476 (2237) (2020) 20190549, http://dx.doi.org/10.1098/rspa.2019.0549.

[23] M.O.T. Cole, P.S. Keogh, Asynchronous periodic contact modes for rotor vibration within an annular clearance, Proc. Inst. Mech. Eng. C 217 (10) (2003) 1101–1115, http://dx.doi.org/10.1243/095440603322517126.

[24] M.S. Akay, A.D. Shaw, M.I. Friswell, Continuation analysis of a nonlinear rotor system, Nonlinear Dynam. 105 (1) (2021) 25–43, http://dx.doi.org/10.1007/s11071-021-06589-8.

[25] E.T. Chipato, A.D. Shaw, M.I. Friswell, Nonlinear rotordynamics of a MDOF rotor–stator contact system subjected to frictional and gravitational effects, Mech. Syst. Signal Process. 159 (2021) http://dx.doi.org/10.1016/j.ymssp.2021.107776.

[26] S. Lahriri, H.I. Weber, I.F. Santos, H. Hartmann, Rotor–stator contact dynamics using a non-ideal drive—Theoretical and experimental aspects, J. Sound Vib. 331 (20) (2012) 4518–4536, http://dx.doi.org/10.1016/j.jsv.2012.05.008.

[27] M. Torkhani, L. May, P. Voinis, Light, medium and heavy partial rubs during speed transients of rotating machines: Numerical simulation and experimental observation, Mech. Syst. Signal Process. 29 (2012) 45–66, http://dx.doi.org/10.1016/j.ymssp.2012.01.019.

[28] C. Wang, D. Zhang, Y. Ma, Z. Liang, J. Hong, Theoretical and experimental investigation on the sudden unbalance and rub-impact in rotor system caused by blade off, Mech. Syst. Signal Process. 76-77 (2016) 111–135, http://dx.doi.org/10.1016/j.ymssp.2016.02.054.

[29] K. Prabith, I.R. Praveen Krishna, Response and stability analysis of a two-spool aero-engine rotor system undergoing multi-disk rub-impact, Int. J. Mech. Sci. 213 (2022) 1–24, http://dx.doi.org/10.1016/j.ijmecsci.2021.106861.

[30] R. Seydel, From Equilibrium to Chaos: Practical Bifurcation and Stability Analysis, Elsevier, New York, 1988.

[31] P. Sundararajan, S.T. Noah, An algorithm for response and stability of large order systems—Application to rotor systems, J. Sound Vib. 214 (4) (1998) 695–723, http://dx.doi.org/10.1006/jsvi.1998.1614.

[32] G. Von Groll, D.J. Ewins, The harmonic balance method with arc-length continuation in rotor/stator contact problems, J. Sound Vib. 241 (2) (2001) 223–233, http://dx.doi.org/10.1006/jsvi.2000.3298.

[33] L. Peletan, S. Baguet, M. Torkhani, G. Jacquet-Richardet, A comparison of stability computational methods for periodic solution of nonlinear problems with application to rotordynamics, Nonlinear Dynam. 72 (3) (2013) 671–682, http://dx.doi.org/10.1007/s11071-012-0744-0.

[34] L. Peletan, S. Baguet, G. Jacquet-Richardet, M. Torkhani, Use and limitations of the harmonic balance method for rub-impact phenomena in rotor-stator dynamics, in: ASME Turbo Expo 2012: Turbine Technical Conference and Exposition, 2012, Volume 7: Structures and Dynamics, Parts a and B, pp. 647–655, http://dx.doi.org/10.1115/gt2012-69450, [Online]. Available: http://dx.doi.org/10.1115/GT2012-69450.

[35] L. Peletan, S. Baguet, M. Torkhani, G. Jacquet-Richardet, Quasi-periodic harmonic balance method for rubbing self-induced vibrations in rotor–stator dynamics, Nonlinear Dynam. 78 (4) (2014) 2501–2515, http://dx.doi.org/10.1007/s11071-014-1606-8.

[36] L. Salles, B. Staples, N. Hoffmann, C. Schwingshackl, Continuation techniques for analysis of whole aeroengine dynamics with imperfect bifurcations and isolated solutions, Nonlinear Dynam. 86 (3) (2016) 1897–1911, http://dx.doi.org/10.1007/s11071-016-3003-y.

[37] M.K. Al-Solihat, K. Behdinan, Force transmissibility and frequency response of a flexible shaft–disk rotor supported by a nonlinear suspension system, Int. J. Non-Linear Mech. 124 (2020) http://dx.doi.org/10.1016/j.ijnonlinmec.2020.103501.

[38] R.M. Rosenberg, The normal modes of nonlinear n-degree-of-freedom systems, J. Appl. Mech. 29 (1) (1962) 7–14, http://dx.doi.org/10.1115/1.3636501.

[39] D. Laxalde, F. Thouverez, Complex non-linear modal analysis for mechanical systems: Application to turbomachinery bladings with friction interfaces, J. Sound Vib. 322 (1009) (2009) 4–5, 1025, http://dx.doi.org/10.1016/j.jsv.2008.11.044.

[40] J. Hong, P. Yu, D. Zhang, Y. Ma, Nonlinear dynamic analysis using the complex nonlinear modes for a rotor system with an additional constraint due to rub-impact, Mech. Syst. Signal Process. 116 (2019) 443–461, http://dx.doi.org/10.1016/j.ymssp.2018.06.061.

[41] D. Liu, J. Hong, Failure analysis of backward whirl motion in an aero-engine rotor, Eng. Fail. Anal. 128 (2021) http://dx.doi.org/10.1016/j.engfailanal.2021.105620.

[42] E.V. Karpenko, M. Wiercigroch, E.E. Pavlovskaia, M.P. Cartmell, Piecewise approximate analytical solutions for a Jeffcott rotor with a snubber ring, Int. J. Mech. Sci. 44 (3) (2002) 475–488, http://dx.doi.org/10.1016/S0020-7403(01)00108-4.

[43] C.A.L.L. Fonseca, I.F. Santos, H.I. Weber, Experimental comparison of the nonlinear dynamic behavior of a rigid rotor interacting with two types of different radial backup bearings: Ball & pinned, Tribol. Int. 119 (2018) 250–261, http://dx.doi.org/10.1016/j.triboint.2017.07.018.

[44] C.A. Fonseca, I.F. Santos, H.I. Weber, Influence of unbalance levels on nonlinear dynamics of a rotor-backup rolling bearing system, J. Sound Vib. 394 (2017) 482–496, http://dx.doi.org/10.1016/j.jsv.2017.01.020.

[45] Y. Cao, H. Yao, Q. Li, P. Yang, B. Wen, Vibration mitigation and dynamics of a rotor-blade system with an attached nonlinear energy sink, Int. J. Non-Linear Mech. 127 (2020) http://dx.doi.org/10.1016/j.ijnonlinmec.2020.103614.

[46] H. Yao, Y. Cao, Z. Ding, B. Wen, Using grounded nonlinear energy sinks to suppress lateral vibration in rotor systems, Mech. Syst. Signal Process. 124 (2019) 237–253, http://dx.doi.org/10.1016/j.ymssp.2019.01.054.

[47] H. Zhang, K. Lu, W. Zhang, C. Fu, Investigation on dynamic behaviors of rotor system with looseness and nonlinear supporting, Mech. Syst. Signal Process. 166 (2022) http://dx.doi.org/10.1016/j.ymssp.2021.108400.

[48] H. Kou, et al., Rub-impact dynamic analysis of a rotor with multiple wide-chord blades under the gyroscopic effect and geometric nonlinearity, Mech. Syst. Signal Process. 168 (2022) http://dx.doi.org/10.1016/j.ymssp.2021.108563.

[49] W. Pan, L. Ling, H. Qu, M. Wang, Nonlinear response analysis of aero-engine rotor bearing rub-impact system caused by horizontal yawing maneuver load, Int. J. Non-Linear Mech. 137 (2021) http://dx.doi.org/10.1016/j.ijnonlinmec.2021.103800.

[50] AUTO-07P: Continuation and bifurcation software for ordinary differential equations, 2019.

[51] T.F. Fairgrieve, A.D. Jepson, O.K. Floquet multipliers, SIAM J. Numer. Anal. 28 (1991) 1446–1462.

[52] J.R. Dorm, P.J. Prince, A family of embedded Runge–Kutta formula, J. Comput. Appl. Math. 6 (1) (1980) 19–26.

[53] P. Varney, I. Green, Rotordynamic analysis of Rotor–Stator rub using rough surface contact, J. Vib. Acoust. 138 (2) (2016) http://dx.doi.org/10.1115/1.4032515.

[54] F. Quinci, W. Litwin, M. Wodtke, R. van den Nieuwendijk, A comparative performance assessment of a hydrodynamic journal bearing lubricated with oil and magnetorheological fluid, Tribol. Int. 162 (2021) http://dx.doi.org/10.1016/j.triboint.2021.107143.